Analysis of LiDAR-derived topographic information for characterizing and differentiating landslide morphology and activity

Nancy F. Glenn [a],*, David R. Streutker [a], D. John Chadwick [b],
Glenn D. Thackray [b], Stephen J. Dorsch [b]

[a] *Department of Geosciences, Idaho State University-Boise, 12301 W. Explorer Dr., Suite 102, Boise, ID 83713, USA*
[b] *Department of Geosciences, Idaho State University, Campus Box 8072, Pocatello, ID 83209-8072, USA*

Abstract

This study used airborne laser altimetry (LiDAR) to examine the surface morphology of two canyon-rim landslides in southern Idaho. The high resolution topographic data were used to calculate surface roughness, slope, semivariance, and fractal dimension. These data were combined with historical movement data (Global Positioning Systems (GPS) and laser theodolite) and field observations for the currently active landslide, and the results suggest that topographic elements are related to the material types and the type of local motion of the landslide. Weak, unconsolidated materials comprising the toe of the slide, which were heavily fractured and locally thrust upward, had relatively high surface roughness, high fractal dimension, and high vertical and lateral movement. The body of the slide, which predominantly moved laterally and consists mainly of undisturbed, older canyon floor materials, had relatively lower surface roughness than the toe. The upper block, consisting of a down-dropped section of the canyon rim that has remained largely intact, had a low surface roughness on its upper surface and high surface roughness along fractures and on its west face (unrelated to landslide motion). The upper block also had a higher semivariance than the toe and body. The topographic data for a neighboring, older and larger landslide complex, which failed in 1937, are similarly used to understand surface morphology, as well as to compare to the morphology of the active landslide and to understand scale-dependent processes. The morphometric analyses demonstrate that the active landslide has a similar failure mechanism and is topographically more variable than the 1937 landslide, especially at scales >20 m. Weathering and the larger scale processes of the 1937 slide are hypothesized to cause the lower semivariance values of the 1937 slide. At smaller scales (<10 m) the topographic components of the two landslides have similar roughness and semivariance. Results demonstrate that high resolution topographic data have the potential to differentiate morphological components within a landslide and provide insight into the material type and activity of the slide. The analyses and results in this study would not have been possible with coarser scale digital elevation models

---

* Corresponding author. Tel.: +1 208 685 6755; fax: +1 208 685 6776.
  E-mail address: glennanc@isu.edu (N.F. Glenn).

(10-m DEM). This methodology is directly applicable to analyzing other geomorphic surfaces at appropriate scales, including glacial deposits and stream beds.

1. Introduction

Landslides cause substantial economic, human, and environmental losses throughout the world. They are often triggered by other natural disasters, such as earthquakes and floods, and are difficult to predict. One of the greatest limiting factors in predicting and mapping landslide activity is the lack of understanding of scale-dependent processes, such as erosion, weathering, and fracturing. The literature on this topic is predominantly theoretical, although several uses of remote sensing and statistics to describe scale and morphometric parameters have been proposed (Bishop et al., 1998, 2003; Bonk, 2002; Phillips, 2005; Wallace et al., 2004). Previous studies have linked landslide processes with morphology and slide components (Smith, 2001; Korup, 2004; McKean and Roering, 2004).

Topographic data with a resolution relevant to the scale of morphological features of the landslide are necessary to understand the space- and time-dependent processes manifested in the slide morphology. Though 10-m digital elevation models (DEMs) are widely available in the U.S., they are not always of sufficiently fine scale for landslide mapping, nor are they widely available for many countries. Numerical analyses of fine scale topography can provide preliminary insight into landslide-scale mechanics and surface deformation (McKean and Roering, 2004). For example, relationships between topographic data and the surface expression of processes may provide insight into landslide activity, age, and material type. Previous studies have linked scale and morphology to weathering (Phillips, 2005), but addressing the problem of spatially and temporally dependent geomorphological mapping of landslides has been challenged by the lack of high-resolution topographic data.

Several techniques have been used to study landslide morphological elements and deformation. Interferometric synthetic aperture radar (InSAR) can provide information on spatial patterns and mechanics of individual landslide blocks, leading to modeling of slide failure (Kimura and Yamaguchi, 2000). Though InSAR has promising potential for understanding temporal deformation of landslides, it is subject to several complicating factors including landslide scale and satellite viewing geometry (Catani et al., 2005). Global Positioning System (GPS) and other point data (e.g., from extensometers) can provide temporal patterns of slide velocity for landslide modeling (Coe et al., 2003). While GPS and InSAR can elucidate slide mechanics and constrain slide models, currently only high resolution laser altimetry topographic data allow for the quantitative geomorphometric analyses necessary to understand spatial scale-dependent processes. Data from small-footprint airborne laser altimetry (light detection and ranging, LiDAR) can provide high resolution topographic information (1 m horizontal and 15 cm vertical accuracy) for geomorphometry (Gold, 2003; Rowlands et al., 2003; Hsiao et al., 2004; McKean and Roering, 2004).

The use of LiDAR for these types of quantitative analyses is relatively new; however, previous studies have used DEM-based geomorphometry for landslide delineation and risk (Gritzner et al., 2001), discriminating zones of surficial processes in mountainous terrain (Bishop et al., 2003), and mapping landforms for structural interpretations (Ganas et al., 2005) and regional analysis (Bolongaro-Crevenna et al., 2004). These analyses typically included first- and second-order derivatives of elevation such as slope angle, slope aspect, profile curvature, tangential curvature, etc. A few studies have used statistical measures such as semivariograms and spatial autocorrelation for geomorphometry, which can provide information about topographic variability and surface roughness (Bishop et al., 1998, 2003; Walsh et al., 2003; Miska and Hjort, 2005).

The purpose of this research is to demonstrate local topographic variability for landform mapping and characterization of two landslides (0.22 and 0.85 km^2 in size) in southern Idaho using LiDAR data.

We examine local topographic variability through measures of topographic roughness (referred to hereafter as surface roughness), slope semivariance and fractal dimension. Specifically, our objectives are to (i) develop the use of surface roughness and slope maps, semivariograms, and fractal dimensions using vector point LiDAR elevation data for identifying patterns in morphology, movement history, and material types for the active, smaller Salmon Falls landslide; and (ii) use these same morphometric parameters (surface roughness, semivariance, fractal dimension) to compare the active slide with the older and larger 1937 landslide. We hypothesize that those components of the currently active landslide that have undergone high degrees of deformation also have high topographic variability and that the landslide morphological components have higher topographic variability than the comparable components of the older landslide.

2. Study area

The Salmon Falls landslide is a canyon-rim landslide along Salmon Falls Creek, a tributary to the Snake River in southern Idaho (Fig. 1). The slide is located ~11 km upstream from the confluence of the Snake River and is ~0.22 km² in area. The slide is part of a larger slide complex along Salmon Falls Creek, an area known as Sinking Canyon. Just north of the currently active landslide within Sinking Canyon is another slide, larger in scale (~0.85 km²) and which failed in 1937.

The Salmon Falls landslide is hypothesized to be a hybrid of a rotational–translational-style slide (Dorsch, 2004) of Lucerne School basalt overlying weak lacustrine and fluvial sediments, both of the Tertiary Glenns Ferry Formation. Movement of the slide was first observed in 1999 and was monitored
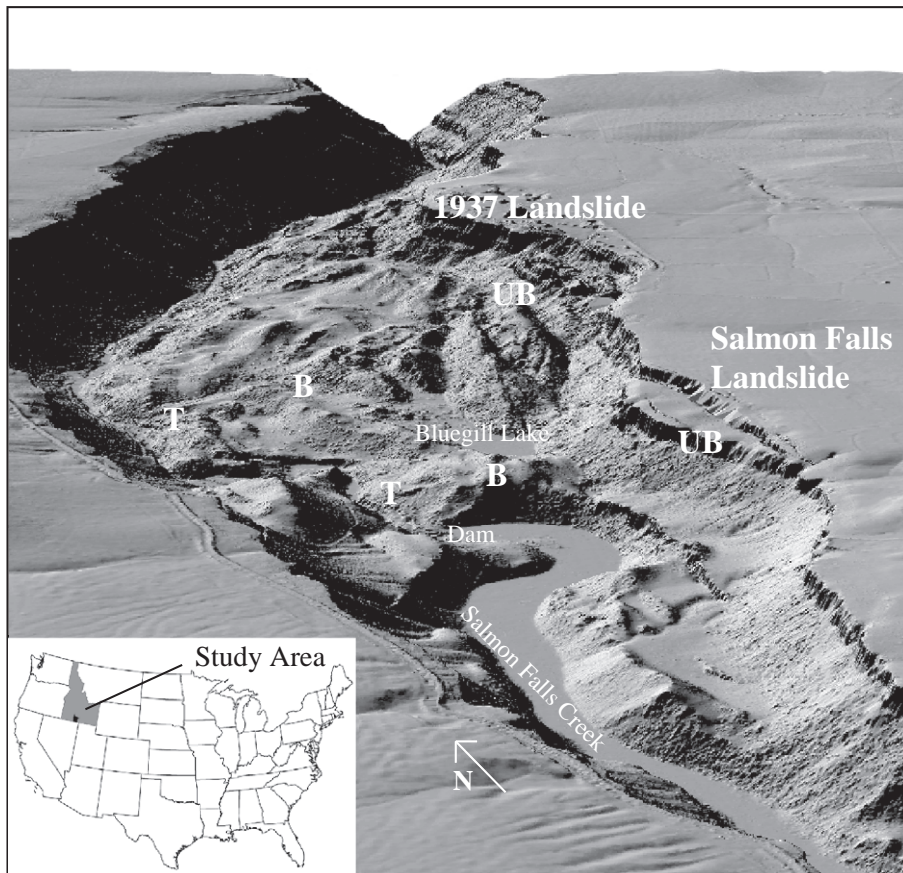

Fig. 1. LiDAR perspective view of Sinking Canyon. UB=Upper block, B=Body, T=Toe.

with laser-theodolite data from 2001 to 2004; GPS data were also used to monitor the slide in 2003 and 2004 (Chadwick et al., 2005).

The Salmon Falls landslide consists of three main morphological components defined in this study: the upper block (~130,000 m^2), main body (~60,000 m^2), and toe (~25,000 m^2) (Fig. 1). The upper block is a portion of the canyon rim and wall that has detached and moved downward and westward into the canyon, and consists of Lucerne School basalt with a series of fractures on the east and west sides. Basalt blocks have littered the slope below, contributing to a steep talus slope on the western side of the upper block. The main body of the slide consists of older landslide debris and canyon floor materials, mostly Lucerne School basalt underlain by Glenns Ferry Formation lacustrine and fluvial sediments. The toe of the slide, also consisting of these weak, unconsolidated materials, has uplifted ~1.25 m and partially dammed Salmon Falls Creek in two locations (Dorsch, 2004). The southernmost dam has resulted in the formation of a ~2-km long lake.

Dorsch (2004) utilized Quickbird multispectral satellite imagery and digitized aerial photographs to perform a change detection analysis between 1990 and 2002 for the Salmon Falls landslide; this study also developed a fracture map showing the pattern of surface deformation of the landslide. The fracture map showed significant fractures at the toe, upper block, and southern boundary of the landslide. The study concluded that the Salmon Falls landslide moved significantly (e.g., 8-m lateral toe movement) prior to the commencement of theodolite monitoring in 2001 and GPS monitoring in 2003. Theodolite monitoring was performed on the landslide by the Bureau of Land Management (unpublished data) and Dorsch (2004) between 2001 and 2004. The theodolite data indicate that the toe of the Salmon Falls landslide had the largest amount of lateral and vertical movement (1 m westward and 1.25 m upward, respectively), the main body had large lateral movement (1.75 m westward) but less vertical movement (5 cm downward), and the upper block had large amounts of lateral and vertical movement (75 cm westward and 1 m downward, respectively) (Dorsch, 2004). Chadwick et al. (2005) utilized five GPS stations to obtain information about subtle changes in movement between February 2003 and March 2004, and converted two-dimen-

sional historical (1990–2002) velocities derived from the Quickbird-air photo analyses to three-dimensional velocities. While the GPS data were collected over a shorter time period, they indicated similar movements to the theodolite data over the corresponding time frame (Chadwick et al., 2005). Ellis et al. (2004) assessed the hazard of further failures of the Salmon Falls landslide and of dam breaching and potential flooding of Salmon Falls Creek. They indicated that catastrophic breaching of the major landslide dam is unlikely given current conditions.

The 1937 slide adjacent to the Salmon Falls slide has not been studied in detail; however, the morphology and failure patterns are similar for both. Lee (1938) proposed that the 1937 slide was caused by Salmon Falls Creek deepening its channel and undercutting the toe. Like the Salmon Falls landslide, fractures are present along the upper portion of the landslide; several basalt masses broke away from the canyon rim at those fractures and slid into the canyon (Fig. 1). These basalt masses are equivalent to the upper block of the Salmon Falls slide in this study. The body consists of weathered basalt blocks and upturned Glenns Ferry Formation lacustrine and fluvial sediments. The toe of the slide consists of the Glenns Ferry Formation lacustrine and fluvial sediments.

3. Methodology

3.1. LiDAR data

LiDAR vector point data were collected over ~17 km^2 of the Salmon Falls landslide and adjacent areas of Sinking Canyon in October 2002. The data were collected with a small-footprint (~25-cm diameter at nadir), 25-kHz infrared laser at a horizontal spacing of ~1 m, resulting in nearly 20 million data points. First and last laser pulse readings were recorded with an elevation, time stamp, and return intensity. The last pulse data were then divided by the vendor into separate bald earth and vegetation classes, with the bald earth vector point data used for subsequent analysis in this study. The absolute vertical accuracy of the LiDAR data, with respect to a standard geographic coordinate system, is 16 cm (95% confidence level), as measured by the vendor using a ground survey of 828 GPS points. The relative or point-to-point vertical

accuracy of the elevation data was found to be on the order of 5 cm. Relative accuracy is determined by measuring the standard deviation of a group of points that are known to form a flat surface. In the case of this study, such calculations were made using the lakes and ponds found within Sinking Canyon. Though infrared lasers generally reflect poorly from water surfaces, the number of returns in the data set was adequate to perform this analysis.

3.2. Geomorphometry

Several techniques are used in this study to examine the landslide morphology expressed in the topographic data within the different landslide components and to evaluate the relationship between surficial expression of landslide morphology, movement rates, and material type. Specifically, the bald earth LiDAR data were used to generate maps of local topographic roughness (surface roughness) and slope, semivariograms for understanding the morphological and scale-dependent characteristics of the topography, and fractal dimensions as a tool for comparing scale-dependent topographic variability of different landslide components. These analyses used the vector point data from the bald earth data set and were performed for both landslides. The vector point data were used in lieu of a DEM in order to preserve the high accuracy of the original data by avoiding the interpolation errors that accompany raster DEM generation.

As stated above, the great value of LiDAR data lies in its high spatial resolution. As such, the focus of this study is topographic variability at fine length scales, such as those of a few meters. This focus led to the development of an algorithm which determines the local topographic variability, or surface roughness, of the LiDAR data. To accomplish this, it was necessary to separate the large scale topography from the fine scale variability. The vector point data were divided into 5×5 m grid cells, each containing 5 to 50 data points, depending on the local density of the data points. Within each cell,
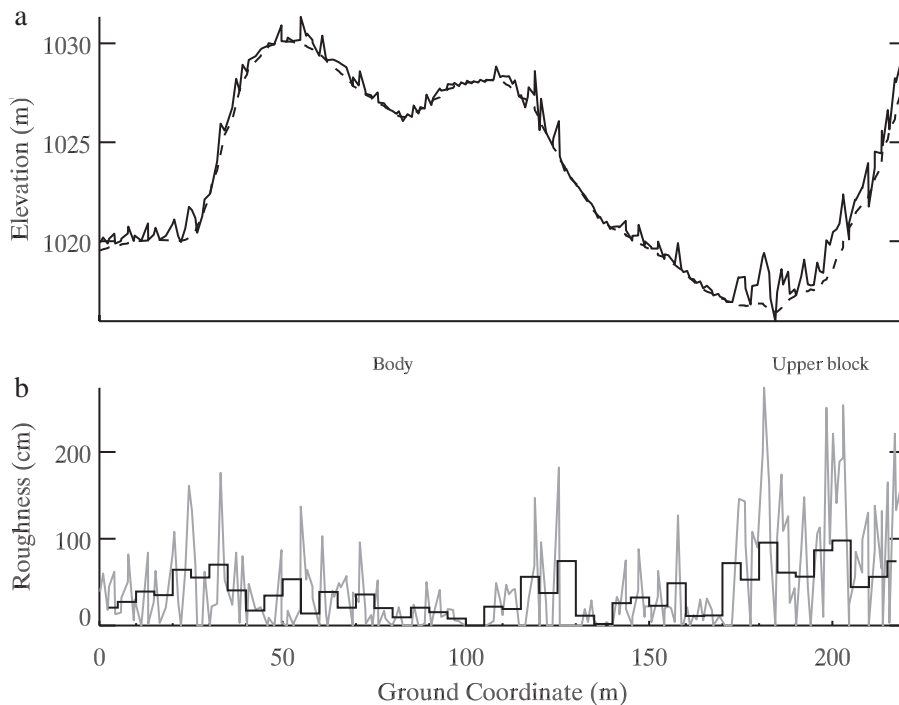

Fig. 2. (a) One-dimensional elevation profile of Salmon Falls landslide. Solid line is bald earth LiDAR data and dashed line is interpolated underlying surface. (b) Grey line is elevation (height) of the data points above the interpolated underlying surface. The black line is the one-dimensional profile of surface roughness, calculated over the 5-m cell intervals.

the point of lowest elevation was selected. These locally low elevation points, with an average spacing of 5 m by virtue of the cell size, were used to interpolate the baseline elevation surface. The interpolation was performed using a thin-plate spline. The height of each remaining data point above this surface was then calculated. The surface roughness of each cell was determined by calculating the standard deviation of these heights above the underlying surface. Such a calculation provides a measure of local surface roughness independent of large-scale topographic variability. The one-dimensional analogue of this process is shown in Fig. 2. Fig. 2a shows a cross-section of the elevation data, where the solid black line represents the vector point data, and the dashed line is the resulting interpolated underlying
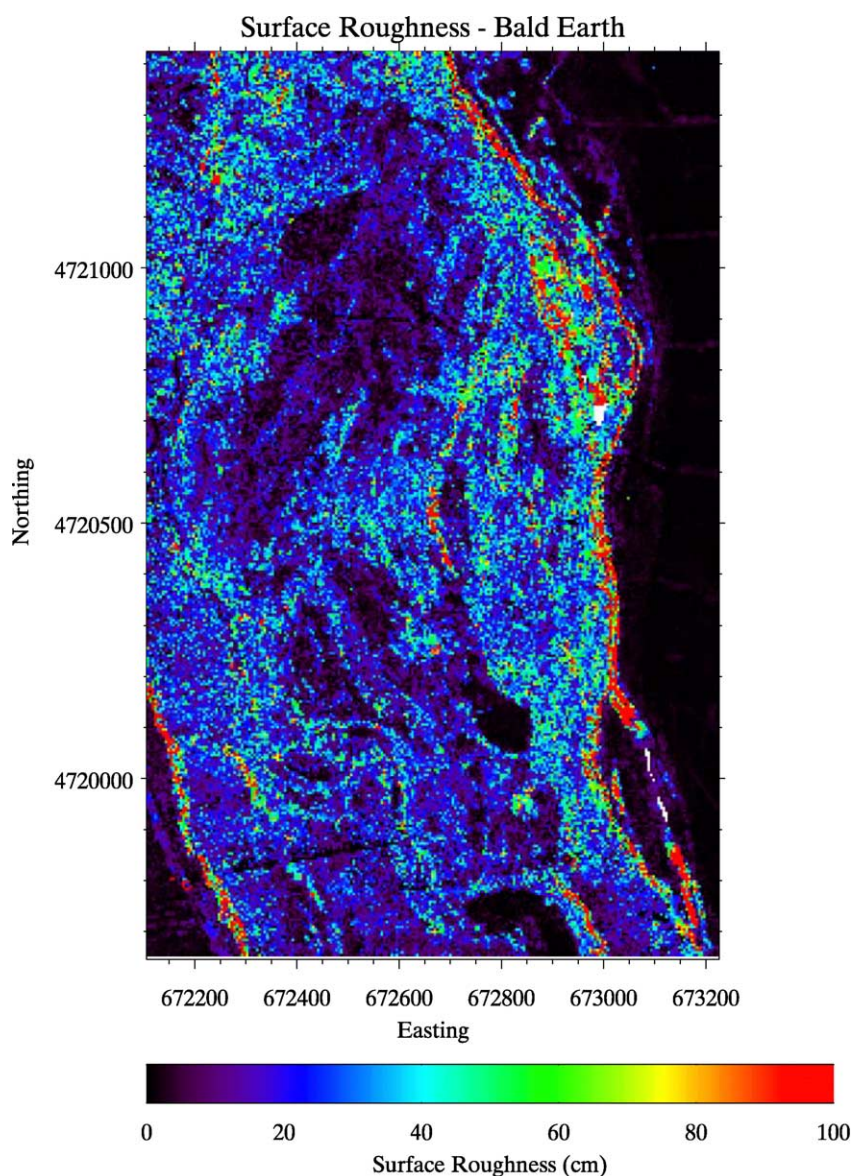

Fig. 3. Surface roughness of Sinking Canyon area. White areas indicate no available data.

surface. Fig. 2b shows the local variability (the large-scale topography having been removed), where the grey line represents the heights of the vector point data above the underlying surface, and the black line shows the surface roughness, calculated as the standard deviation over the 5-m intervals. The 5-m width was chosen for the grid cells in order to include a sufficient number of data points for the calculation while maintaining a relatively high spatial resolution. The resulting surface roughness value (Fig. 3) of each grid cell is thus the average topographic variability over length scales from approximately one meter (the horizontal spatial resolution of the LiDAR data) to 5 m (the size of the cell).

The map of slope values (Fig. 4) was calculated in a manner similar to the surface roughness map. The
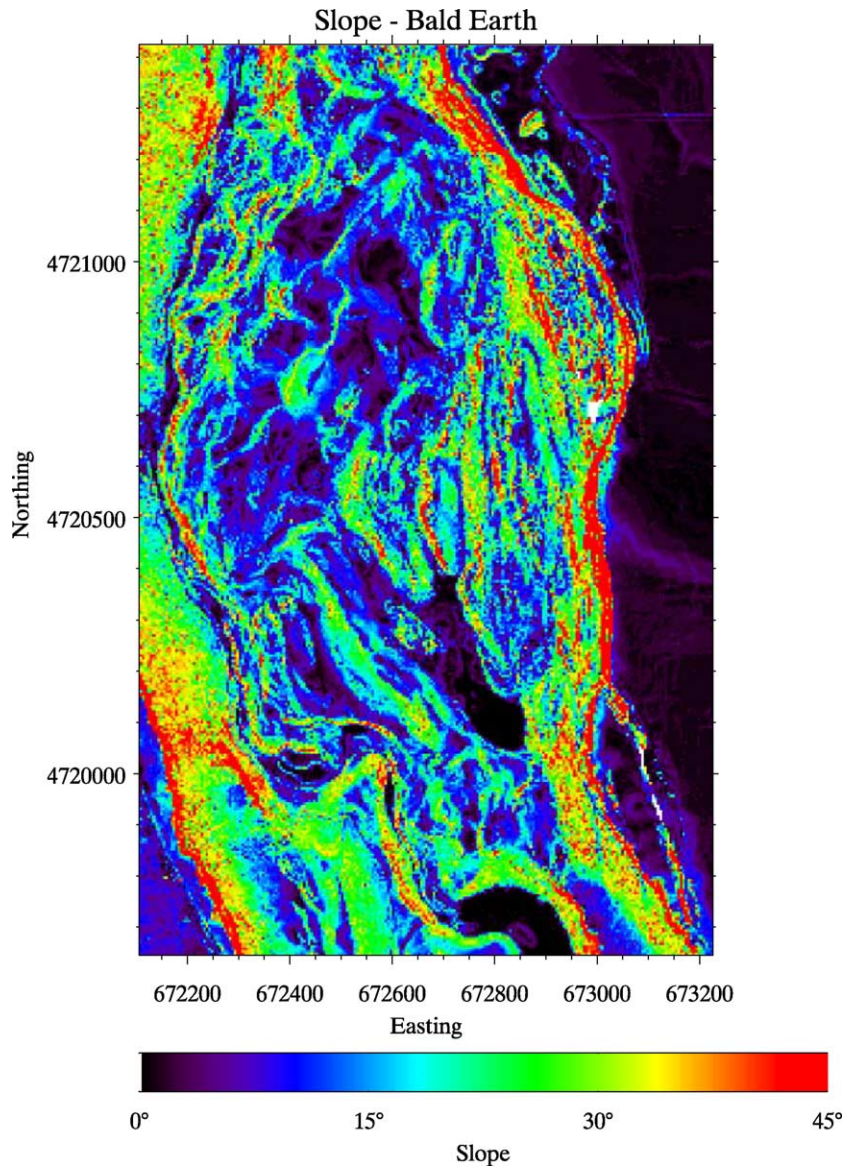

Fig. 4. Slope of Sinking Canyon area. White areas indicate no available data.

point vector LiDAR data were again divided in 5×5 m grid cells. The overall gradient (in both the x- and y-directions) of the points in each cell was calculated, and the slope value of each cell was found by summing the two gradient components.

Two-dimensional semivariograms were generated for sample locations (Fig. 5) in each of the main landslide components to examine relative spatial variability of the topography. Following Carr (1995), the two-dimensional semivariogram is expressed as

$$\gamma(h) = (1/2n) \sum \left[Z(x_i, y_i) - Z(x_{i+h}, y_{i+h}) \right]^2 \qquad (1)$$

where $\gamma(h)$=semivariance at lag distance h; $Z(x_i, y_i)$=data value at location i; $Z(x_{i+h}, y_{i+h})$=data value at location i plus distance h; and n=number of samples in the data set. In this study, Z represents the vector point elevation obtained from the bald earth data set.

The shape of the semivariogram plot describes the spatial dependence between samples Z as a function of distance h. If there is spatial dependence within the data, $\gamma(h)$ typically increases with separation distance h, and may level off or even decrease after a certain distance. The range of the semivariogram is the lag distance at which the semivariance reaches a plateau and spatial autocorrelation between samples no longer exists (Fig. 6). This range corresponds to the ceiling of the semivariogram, called the sill, and is often equal to the statistical variance of Z. The nugget is the value of the semivariance at zero lag distance and is obtained by extrapolating the plot back to the origin. A nonzero nugget value provides an indication of the amount of noise in the data set or an indication of a microspatial autocovariance at a scale below the sampling resolution (Carr, 1995). In essence, the semivariograms are used to show spatial trends in the topographic data (variability in relief) over different spatial scales (lag distances).

The semivariograms were computed for the toe, body, and upper block of both landslides using Visual_Data, a Windows-based Visual Basic program (Carr, 2002). The number of samples (elevation postings) included 5322 for the toe, 32,223 for the body, 20,781 for the upper block of the currently active slide and 32,974 for the toe, 32,653 for the body, and 79,222 for the upper block of the 1937 landslide. The largest possible number of samples was included in each data
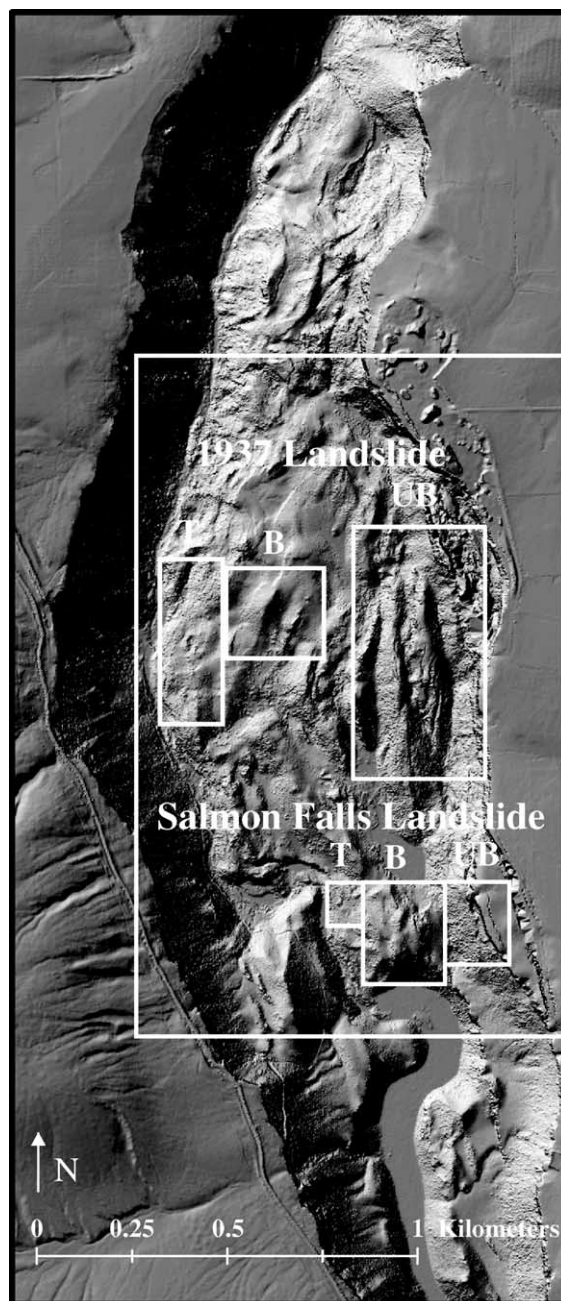

Fig. 5. Subsets of 1937 and Salmon Falls landslides for semivariogram and fractal analyses. Outer box is area used for surface roughness and slope in Figs. 3 and 4, respectively. UB=Upper block, B=Body, T=Toe.

set in order to characterize the overall topography without sample size bias. The sample locations used for the semivariogram and fractal analyses for the 1937
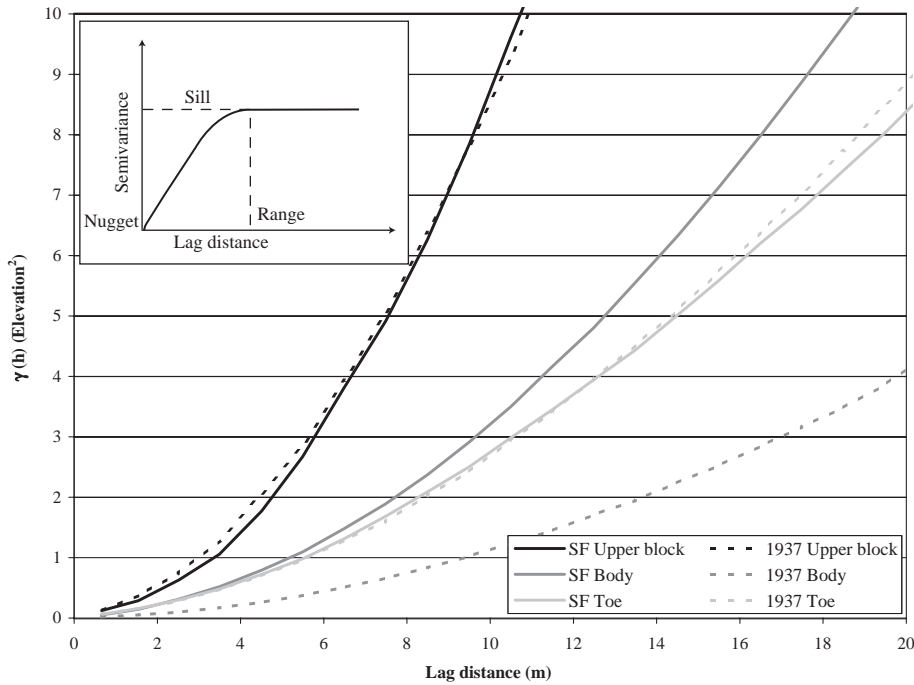
Fig. 6. Semivariograms for Salmon Falls and 1937 landslides at lag distances <20 m. Inset is a graphical display of a spherical semivariogram model.

slide were chosen to best represent equivalent features in the currently active slide. The semivariograms were plotted to a lag distance equal to ~50% of the smaller

Table 1
Statistical moments of landslide components

	Toe	Body	Upper block
Salmon Falls Landslide			
Number of LiDAR Samples	5322	32,223	20,781
N–S dimension (m)	113	273	216
E–W dimension (m)	94	240	169
Elevation minimum (m)	981.45	986.38	1011.21
Elevation maximum (m)	1014.13	1047.34	1098.10
Elevation range (m)	32.68	60.96	86.89
Elevation mean (m)	997.10	1016.16	1068.01
Elevation variance (m^2)	44.50	104.46	822.61
1937 Landslide			
Number of LiDAR Samples	32,974	32,653	79,222
N–S dimension (m)	185	236	659
E–W dimension (m)	187	257	345
Elevation minimum (m)	950.78	986.33	1003.07
Elevation maximum (m)	1001.72	1021.15	1104.08
Elevation range (m)	50.94	34.82	101.01
Elevation mean (m)	979.94	1005.83	1035.31
Elevation variance (m^2)	119.16	74.46	368.68

size dimension of the sample. Two-dimensional omni-directional semivariograms were computed, averaging over all spatial directions, for each of the landslide components. Omnidirectional semivariograms were chosen over directional semivariograms in order to compare the relative average spatial patterns within each landslide component. The range, mean and variance of each of the subsets were also computed to compare to the semivariograms (Table 1).

Topographic data can be described as self-affine random fractals (Turcotte, 1997), allowing fractal dimension to be used to understand the topographic roughness. In general, the greater the fractal dimension of the surface, the "rougher" the surface is. The fractal dimensions were computed in this study for understanding the degree of complexity and spatial autocorrelation in the topography. Fractal dimensions were computed using the semivariogram method where the fractal dimension D is estimated by

$$D = 3 - m/2 \qquad (2)$$

where m = the slope derived from the $\log(\gamma(h))$ versus $\log(h)$ plot. The log–log plots were examined for

multi-fractality, as signified by scale-breaks (changes in the slope, and therefore in fractal dimension). In order to verify linearity in the log–log plots, R^2 values were computed. Fractal dimension was computed from the slope between each data point, starting at the lowest lag and ending at the lag distance where the first break in slope occurred (R^2 value lower than 0.99). The fractal dimension was not computed beyond a lag distance of ~20 m for the body of the currently active landslide and 90 m and 30 m for the body and upper block, respectively, for the 1937 landslide because of scale-breaks. More information detailing methods on computations of fractal dimension can be found in Carr (2002) and Carr and Benzer (1991).

4. Results

4.1. Surface roughness and slope

Although the absolute accuracy of the LiDAR data is 16 cm, relative accuracies of a few centimeters allow for the computation of surface roughness values that are less than the absolute accuracy. The surface roughness values for the Salmon Falls and 1937 land-slides range from <5 cm to >1 m with higher surface roughness near the toes of the slides and the fractured edges of the upper blocks. Lower surface roughness is exhibited in the relatively undeformed body of each slide and the upper surface of the upper block of the currently active landslide (Fig. 3). Within the active landslide, surface roughness ranges from <5 to 100 cm for the upper block (reflecting the inclusion of both the flat, undeformed surface and the talus slope at the western edge), 5 to 50 cm for the main body (with localized areas up to 100 cm), and ~40 to 100 cm for the toe. In the 1937 slide area, the numerous ridges that comprise the upper block region have high surface roughness values (20–100 cm), grading to lower surface roughness values in the main body of the landslide debris (<40 cm). Surface roughness increases near the toe of the slide, with values up to 100 cm (Fig. 3).

The slope calculation (Fig. 4) resulted in high slopes for several portions of the upper block region and, to a lesser degree, toe area comprised of Glenns Ferry sediments in both landslides. The failed upper blocks of the 1937 slide and the upper block of the currently active landslide have slopes up to 45°. Failed basalt blocks in the body of the 1937 slide also form ridges of high slopes (30° to 45°) that are oriented to the NW in the northern portion, to the west in the main portion, and to the SW in the southern portion of the slide. The toes of both slides have high slopes (up to 45°) consisting of overstee-pened sediments.

4.2. Semivariograms

The shape of the semivariograms for the toe, body, and upper block of the currently active landslide are similar to a parabolic form, indicative of continuity of the elevation variable (Figs. 6 and 7). At short lag distances (<20 m) the semivariance of the upper block is larger than that of the body and toe. At lag distances >20 m the semivariance of the upper block appears to have no limit: the elevation properties have no finite variance (the semivariogram is unbounded). Overall the semivariance of the upper block indicates high variability in the topographic data over spatial scales of ~50 m. The body semivariance is slightly larger than that of the toe, with increasing difference between the two with increasing lag distance; how-ever, the semivariance of the toe supersedes that of the body at a lag distance of ~70 m and rises to a sill at a range of ~85 m. This indicates that beyond ~85 m there is no longer a spatial relationship between the topographic data. Note that the toe semivariogram is plotted at lag distances over the 50% break-point of data pairs (~50 m) for comparison with the other data sets. The semivariance of the body nearly reaches a sill at a lag distance of ~130 m, indicating that beyond this distance there is little spatial autocorrelation in the topographic data.

The semivariograms of the 1937 landslide also have a parabolic form at short lag distances (<20 m) and none reach a sill (Figs. 6 and 7). The upper block has the largest semivariance of the 1937 plots and is very similar to the semivariogram for the upper block of the currently active landslide at lag distances <20 m. At lag distances larger than ~20 m, the semivar-iance of the 1937 upper block is lower than that of the currently active landslide indicating that at this spatial scale, the topography of the 1937 upper block is more uniform. The semivariance of the toe of the 1937 slide
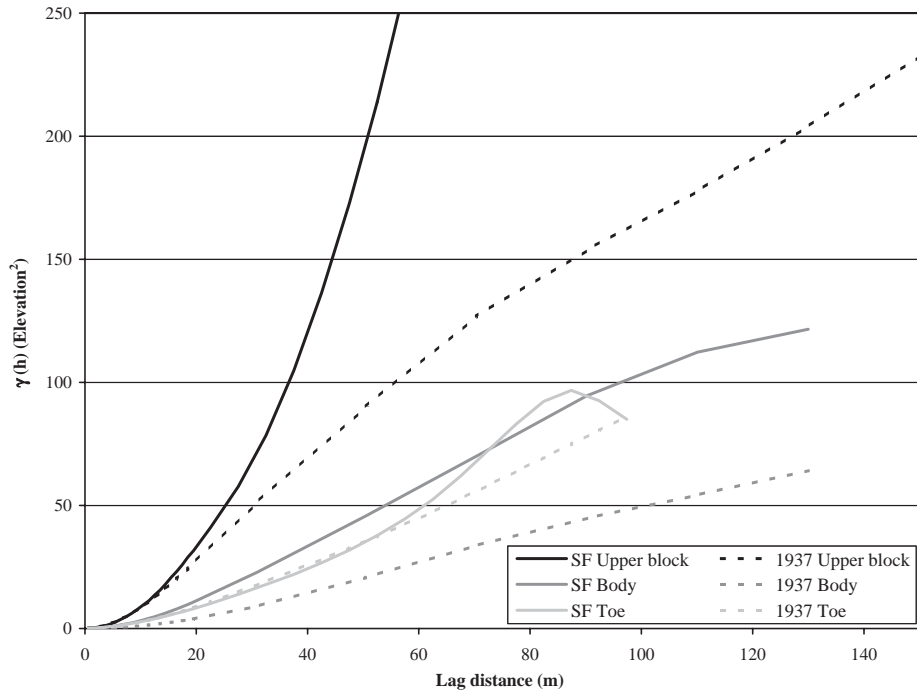
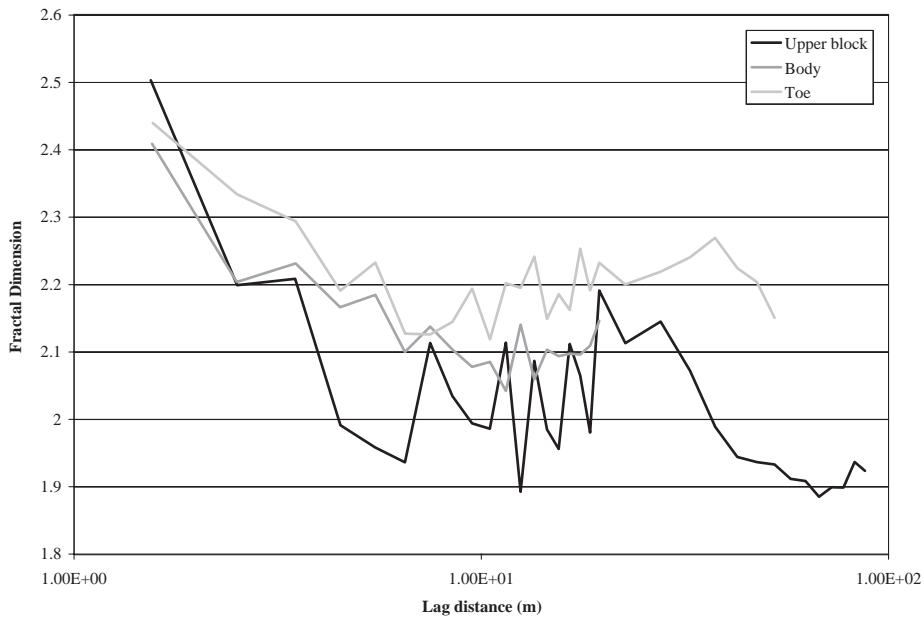Fig. 7. Semivariograms for Salmon Falls and 1937 landslides.

Fig. 8. Fractal dimensions for the Salmon Falls landslide.

is very similar to that of the toe of the active landslide; however, it does not reach a sill and appears to continue to rise with larger lag distances. The semivariance of the 1937 body is the lowest, indicating similar topographic data at a larger spatial scale (lag distance) than the other data sets.

4.3. Fractal dimension

Fractal dimensions were plotted against h (Figs. 8 and 9). In general, the fractal dimension of the toe is higher than that of the body and upper block of the currently active landslide, ranging from approximately 2.45 to 2.15. The fractal dimension of the upper block dips below 2.0 (fractal dimensions of surfaces are expected to be between 2 and 3) at several lag distances (e.g., 5 and 50 m). This result is not surprising because the calculation of fractal dimensions using the semivariogram method is a function of slope and the log–log semivariogram is steep (over 2) in these areas. These values are retained herein for descriptive purposes; further discussion of fractal values beyond expected limits can be found in Carr and Benzer (1991). Similar to the active landslide, the fractal dimension of the toe is greater than that of the body and upper block of the 1937 landslide; however,

at h of ~10 m, the fractal dimension of the upper block increases and is higher than both the toe and body. The fractal dimension varies widely with lag distance; however, in both data sets, lower fractal dimensions occur near h of ~10 m.

5. Discussion

5.1. Comparisons between currently active and 1937 landslides

The surface roughness calculations and field observations of the currently active landslide indicate that the upper block and toe have relatively higher topographic variability than the body at scales relevant to the landslide components (~5 to 130 m). The semivariograms indicate a higher semivariance (and lower spatial autocorrelation) for the upper block than for the body and toe at the modeled lag distances of the active slide. While the high semivariance isn't a direct measurement of surface roughness, it does indicate a lack of similarity between topographic values in the upper block. The upper block is defined by the stark differences between the west talus slope and the smooth, but fractured upper surface. The
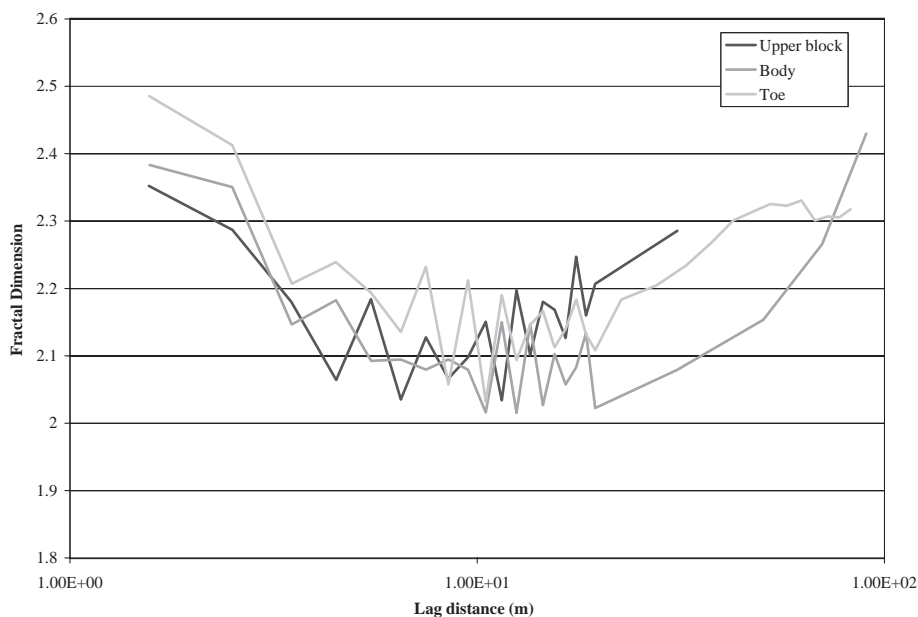

Fig. 9. Fractal dimensions for the 1937 landslide.

semivariance of the toe is lower than the body of the active slide, consistent with the comparison of statistical variance; however, at a scale of ~85 m, the toe semivariance exceeds that of the body, indicating a lower spatial autocorrelation in the toe topographic data. While the high surface roughness from the LiDAR imagery and field observations of upturned sediments in the toe indicate deformation and roughness at small scales (~5 m), the semivariance is lower than that of the smoother body. The semivariogram of the body has a larger range and sill than the toe, indicating lower spatial autocorrelation at larger lag distances. This is interpreted as higher spatial variability as a function of distance in the topographic data and shouldn't be correlated to simply higher surface roughness. Field, theodolite, and GPS observations show little vertical movement or fracturing on this part of the slide, yielding lower surface roughness values.

The fractal dimensions can also be considered a measure of the "roughness" of the topography (Klinkenberg, 1992; Lifton and Chase, 1992; Carr, 1995). The highly variable fractal dimension data set in this study is somewhat ambiguous; yet still useful for relative comparisons between landslide components. For example, while the fractal dimension of the toe is larger than the body and upper block for both landslides (indicating a "rougher" surface), the fractal dimension of the body is also higher than that of the upper block in the currently active slide. The steep slope of the upper block semivariograms result in low fractal dimensions for both slides. The smoother upper surface of the upper block in the active slide may outweigh the influence of the rough west-facing talus slope when comparing to the body. These results indicate that though relative comparisons may be made between data sets, caution should be exercised in correlating fractal dimension to a "rough" or "smooth" topography.

The weak unconsolidated toe material has a higher surface roughness than many areas of the body in the active slide. This portion of the landslide also demonstrated the highest vertical and lateral motion during the time of monitoring, resulting in greater disruption of the surface. The surface roughness is inherently linked to the material type and type of motion (upward thrusting versus lateral sliding). As the upper block drops down and away from the canyon

wall, the body and the toe are pushed westward. The material of the toe is confined by the west canyon wall, which causes the slide to be thrust upward there. The sediments in the toe are weak, and as this motion is inherently disruptive to the surface, it results in large cracks and a rough, uneven surface. The main body, composed of canyon floor and canyon wall materials that have remained largely intact because of the primarily lateral motion of this part of the slide, has a smoother surface than the toe and the upper block. The steep talus slope of basalt on the western unconfined side of the upper block and the fractures within the upper block result in high surface roughness. However, the high surface roughness on the west face is related to rockfall processes independent of the landslide motion. Though not instrumented, this area of the upper block likely had similar movement patterns as the flat, instrumented surface. The low fractal dimension of the upper block is likely the result of the difference between the disaggregated canyon wall basalt and the upper intact surface of the block. The upper block exhibited significant downward motion and slightly less lateral motion. The motion and the unconfined west face of the upper block resulted in high topographic variability along the west face and in highly fractured areas (Fig. 10).

The fracture patterns of the active landslide (Dorsch, 2004) are consistent with the surface roughness maps, as areas with tension cracks and fractures (specific locations on the toe and upper block) also have high surface roughness (Fig. 10). The unconsolidated material of the toe leads to large cracks and high surface roughness. The fractures in the basalt of the upper block also result in localized high surface roughness. The tension cracks and fractures near the southern edge of the landslide are less distinct in the surface roughness map, likely because of the small size of the cracks and the lack of vertical offset on these primarily strike-slip fractures.

The data from the 1937 slide reveal similar patterns to those from the active landslide; however, movement data are not available to correlate to surface roughness and spatial patterns in the topographic data. Furthermore, the 1937 slide is approximately four times as large, resulting in larger spatial characteristics and patterns that make comparisons challenging. This example of scale dependency is one of the most important aspects in linking landslide processes
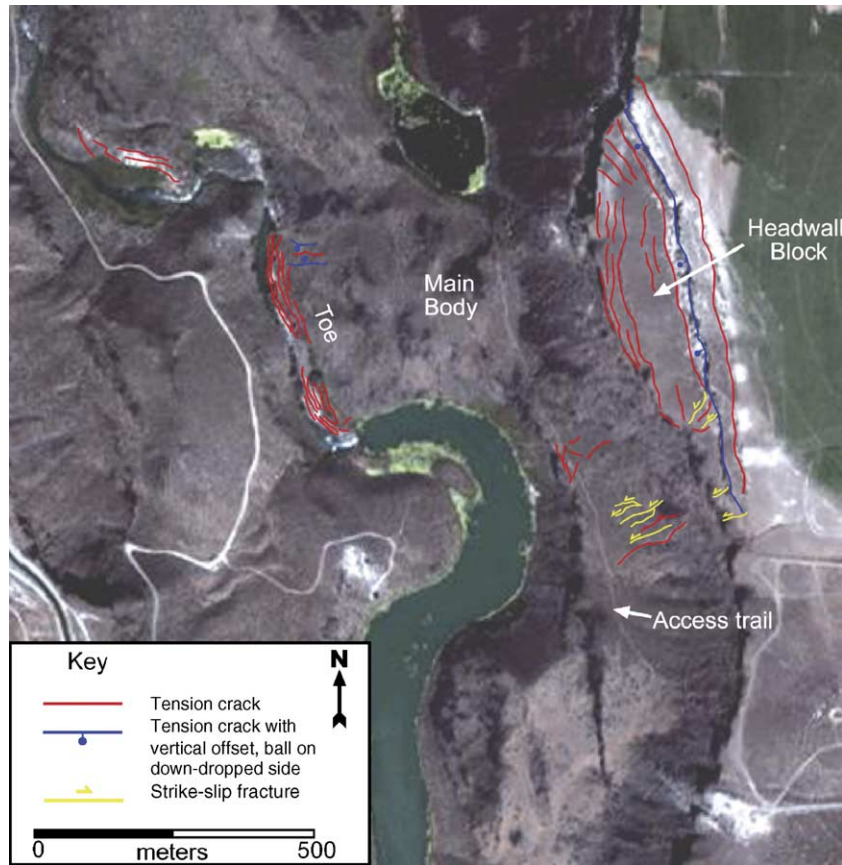
Fig. 10. Fracture map from Dorsch (2004). Tension cracks and fractures on upper block and toe correspond to high surface roughness areas in Fig. 3. Cracks and fractures near access trail are not as easily identified in Fig. 4.

to morphology. And while this study uses the 1937 landslide as a comparative feature to the active slide, the comparative parameters (e.g., surface roughness) can be used as first-step mapping tool (Fig. 11).

In comparison to the active landslide, the 1937 toe has a similar surface roughness and semivariance at short lag distances. At larger lag distances the semi-variogram of the toe has a shallower slope, demonstrating slightly higher spatial autocorrelation at larger scales (60–100 m). The broader toe (and topographic expression) of the 1937 slide is likely from secondary slumping in the toe sediments. The LiDAR derived surface roughness of the body of the 1937 slide is lower and more uniform than that of the active slide. For example, the surface roughness of the 1937 slide's body is consistently <40 cm, while some areas of the body of the active landslide have surface roughness

values as large as 100 cm. The higher surface rough-ness values of the active landslide are expected, given the younger age of the slide, and likely result from less weathering and surface erosion as well as less dust deposition and organic accumulation. This implies that surface roughness may be one method to assess relative ages between slides that have similar material types. The semivariogram of the body of the 1937 slide demonstrates lower spatial autocorrelation than the active landslide at all modeled scales, indi-cative of low spatial variability of the topographic data. As expected, the elevation variance of this subset is also smaller than that of the toe and upper block (Table 1). The repetitive down-dropped blocks of the canyon wall in the 1937 slide display similarly high surface roughness in the LiDAR-derived data as the upper block (largely still intact) of the active slide.
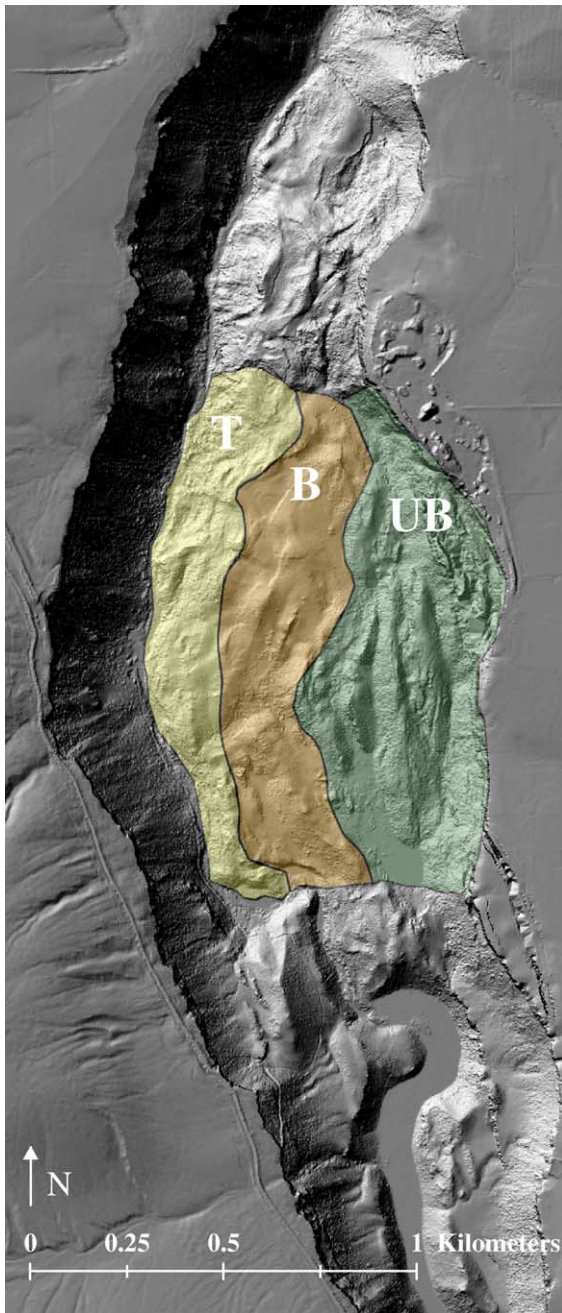
Fig. 11. Mapped boundaries of the toe, body, and upper block regions of the 1937 slide. UB=Upper block, B=Body, T=Toe.

Salmon Falls slide. The repetitive pattern of down-dropped upper blocks was captured in the sample used for the semivariogram. However, samples used in the semivariogram calculations that were taken near the canyon wall where the topography has higher variability resulted in nested semivariograms (not shown) and are examples of the location- and scale-dependency of semivariograms. As the fractures in the upper block and canyon rim of the active slide continue to cut back towards the east, we expect the upper block will attain a statistically similar morphology to that of the 1937 slide. This type of spatial information, especially over time, can provide inferences about the age and movement activity of landslides. The challenge is quantitatively relating changes in properties of topography with landslide age and rates of motion. These relationships hold promising information for understanding landscape development on both a "local" and "regional" level for landslide and other geomorphic processes (e.g., erosion, weathering; see Phillips, 2005). However, comparative analysis is complicated by the scale-dependent processes.

As with the active landslide, the fractal dimensions of the 1937 slide are higher in the toe than in the body. Furthermore, the fractal dimensions for the toe and body are slightly smaller than those for the active landslide. The fractal dimension of the upper block does exceed that of the body and toe at high lag distances (>10 m) in the 1937 slide. This result can be observed in Fig. 5, where the upper block consists of at least three down-dropped blocks with rough west faces in comparison to the smoother, lower frequency ridges of the body.

The surface roughness, semivariance, and fractal dimension results indicate that the active landslide is similar in topographic expression to the older landslide. The surface roughness values for each of the landslide components are comparable between the two slides. Even visual interpretation of the surface roughness (Fig. 3) of both slides distinguishes between the rougher upper blocks, smoother areas in the main bodies, and rougher toes. The high surface roughness ridges in the older slide are equivalent to westerly rotated versions of the upper block in the active slide. These segments were originally flat with rough west talus faces, but were then rotated on a listric plane. The western edges of these ridges are equivalent to the west face of the upper block on the

The 1937 upper blocks detached and moved rapidly away from the canyon wall, resulting in larger-scale rock fall and more extensive fracturing than in the

active slide and the smoother east sides of these ridges are equivalent to the surface of the upper block. From this we can expect the upper block of the active slide to rotate and form a tilted ridge. Likewise from studying the 1937 slide and understanding the motion of the active slide, we can expect the body of the active slide to remain intact and smooth with increased weathering, erosion and dust deposition. The slope-generated data (Fig. 4) indicate that failed basalt rims in the 1937 slide, and to a lesser degree Glenns Ferry sediments in both slides, have steep slopes. The basalt rims in the 1937 slide provide information about the scale of fracturing and failure. The rims are oriented NW and W, indicating the orientation of fractures in the basalt on which motion initiated. These rims are ~400 m in length from north to south. This is comparable to the upper block of the active landslide (500 m), further indicating that the younger landslide is likely demonstrating similar failure mechanics as the 1937 slide.

Results of semivariogram analyses indicate that, in general, the active slide has a higher semivariance and lower degree of spatial autocorrelation than the older slide. While there are some exceptions to this (e.g., at lag distances <8 m in the upper blocks and lag distances between 12 and 50 m for the toes), the differences in semivariance between the slides at these lag distances are very small. These findings indicate that the active slide has higher topographic variability as a function of distance. This can be explained by the smaller scale processes of the landslide and the younger age in comparison to the 1937 slide. These results indicate that the semivariograms can be useful for relative assessments of processes and age between landslides.

The fractal dimension results also indicate potential for classifying between landslide scales and ages. As previously stated, fractal dimensions of the body and toe of the 1937 slide are smaller than comparable components of the active slide at a scale near 10 m. Yet this doesn't hold true for the upper block where the steep semivariance results in extremely low fractal dimensions in the active slide. We may expect the fractal dimensions to become more similar between the two slides over time at small scales (~10 m), as the semivariograms of the active slide become closer to those of the 1937 slide. Because our analysis of fractal dimension was based on our 2-D semivariograms, the

fractal dimensions represent a surface (rather than a profile). For our purposes, using fractal dimension to demonstrate the relative difference in topographic relief patterns (in space) between landslide components and between older and younger landslides, the semivariogram analyses were sufficient. Alternative methods, such as using the spectral-wavelength plot of a two-dimensional spectral analysis to discern smooth, unfailed terrain from relatively rougher failed terrain, could also be useful (McKean and Roering, 2004).

5.2. Linkages between motion, material, and topography

Our first hypothesis, that the high motion areas of the active landslide were linked to high surface roughness, was valid for the toe. Additionally, portions of the upper block have a high surface roughness due to landslide related fracturing. However, the west talus face of the upper block has the highest surface roughness in the landslide area, but its roughness is a result of rockfall rather than landslide motion. With this important exception, the study indicated that both type of motion and type of material play key roles in the surface expression and resulting surface roughness. Our second hypothesis, that the 1937 slide had a lower or "smoother" surface roughness than the active slide, was proven correct through the surface roughness calculations. Further, because we found that material type, motion, and surface roughness were linked, the comparisons between the landslide data sets are significant for mapping the 1937 slide. The lithology and canyon rim slopes of the 1937 slide are similar to the active slide. These similarities, coupled with the results of the numerical analyses of the topography, allowed us to provide a provisional map of the toe, body, and upper block boundaries of the 1937 slide (Fig. 11). Note that the upper block comprises many of the failed basalt blocks originating from the canyon wall. The northern boundary of the slide is difficult to discern because of another canyon rim slope failure just to the north. Likewise, the southern boundary of the 1937 slide in relation to the northern boundary of the active slide is obscure. More detailed analyses such as edge and linear effects in the topographic data could be explored to help map these boundaries with more confidence.

6. Conclusions

High spatial resolution, bald earth LiDAR data provide new opportunities for mapping landslide morphology through visual interpretation and numerical analysis. Surface roughness and slope calculations, semivariogram analysis, and fractal dimension all provide insight into the landslide morphology and linked slide processes. The results of this study show that topographic data with postings of 1 m or less are appropriate to conduct these analyses on landslides similar in size to the active Salmon Falls landslide. Vertical resolution on the order of 5 cm must be available to depict subtle changes in surface roughness of landslide components. Caution must be exercised when using semivariance and fractal dimensions to understand topographic variability because sample location and scale affect results. However, these tools provide useful relative comparisons of topographic expression in order to understand scale-dependent processes. Our topographic analyses indicate that different morphological components of the currently active landslide have different measurable, but comparable, surface characteristics, likely because of the type of material (e.g., weak sediments vs. intact basalt) and type of motion (e.g., disruptive thrusting and fracturing in the toe vs. the coherent down-dropping of the upper block). High rates of vertical and lateral motion were correlated with both the weak, unconsolidated toe materials having high surface roughness, as well as with the basalt upper block having both low (e.g., upper surface) and high (e.g., fractures and talus slope) surface roughness. However, the high surface roughness of the talus slope is not a function of landslide motion or activity. While the upward motion of the weak toe resulted in a rough disruptive surface, the downward motion of the upper block resulted in a smooth surface with rough fractures. Smaller vertical motion and less surface disruption were associated with a relatively smoother topography in the body. The topographic analysis also indicates that the active landslide has a similar failure mechanism to that of the 1937 slide. Though in situ movement data are not available for the 1937 slide, the statistical analysis for the toe and main body produced similar results as those for the active landslide. The blocks of the 1937 slide that dropped from the canyon rim provided a rougher morphology than the upper block of the active landslide. This information allowed us to map the toe, body, and upper blocks of the 1937 slide without large amounts of field reconnaissance and ground instrumentation. Though the 1937 slide is much larger in scale, the topographic expression provided by the LiDAR data helps to link related processes between the two landslides. High resolution topographic data have the potential to differentiate failure zones within a landslide and provide insight into the material type and movement. This type of analysis is also relevant to other geomorphic applications, such as understanding stream bed topography, fluvial terrace morphology, and glacial landform degradation.

Acknowledgements

References

Bishop, M., Shroder, J., Hickman, B., Copland, L., 1998. Scale-dependent analysis of satellite imagery for characterization of glacier surfaces in the Karakoram Himalaya. Geomorphology 21, 217–232.

Bishop, M., Shroder, J., Colby, J., 2003. Remote sensing and geomorphometry for studying relief production in high mountains. Geomorphology 55, 345–361.

Bolongaro-Crevenna, A., Torres-Rodríguez, V., Sorani, V., Frame, D., Ortiz, M.A., 2004. Geomorphometric analysis for characterizing landforms in Morelos State, Mexico. Geomorphology 67, 407–422.

Bonk, R., 2002. Scale-dependent geomorphometric analysis for glacier mapping at Nanga Parbat: GRASS GIS approach. Proceedings of the Open Source GIS - GRASS Users Conference 2002, Trento, Italy, pp. 1–4.

Carr, J.R., 1995. Numerical Analysis in the Geological Sciences. Prentice-Hall, New Jersey.

Carr, J.R., 2002. Data Visualization in the Geosciences, Accompanied by Visual_Data CD-Rom. Prentice-Hall, New Jersey.

Carr, J.R., Benzer, W.B., 1991. On the practice of estimating fractal dimension. Mathematical Geology 23 (7), 945–958.

Catani, F., Farina, P., Moretti, S., Nico, G., Strozzi, T., 2005. On the application of SAR interferometry to geomorphological studies: estimation of landform attributes and mass movements. Geomorphology 66, 119–131.

Chadwick, J., Dorsch, S., Glenn, N., Thackray, G., Shilling, K., 2005. Application of multi-temporal high resolution imagery and GPS in a study of the motion of a canyon rim landslide. ISPRS Journal of Photogrammetry and Remote Sensing 59, 212–221.

Coe, J., Ellis, W., Godt, J., Savage, W., Savage, J., Michael, J., Kibler, J., Powers, P., Lidke, D., Debray, S., 2003. Seasonal movement of the Slumgullion landslide determined from Global Positioning System surveys and field instrumentation, July 1998–March 2002. Engineering Geology 68, 67–101.

Dorsch, S., 2004. The geologic framework, movement history and mechanics of the Salmon Falls landslide, Twin Falls County, Idaho. M.S. Thesis, Idaho State University, Pocatello, Idaho.

Ellis, W.L., Schuster, R.L., Schulz, W.H., 2004. Assessment of Hazards Associated with the Bluegill Landslide, South-central, Idaho. U.S. Geological Survey Open File Report 2004–1054. USGS, Denver, CO.

Ganas, A., Pavlides, S., Karastathis, V., 2005. DEM-based morphometry of range-front escarpments in Attica, central Greece, and its relation to fault slip rates. Geomorphology 65, 301–319.

Gold, R.D., 2003. A comparative study of aerial photographs and LiDAR imagery for landslide detection in the Puget Lowland, Washington. Geological Society of America, Cordilleran Section, 99th Annual Meeting, Geological Society of America, vol. 35 (4), p. 12.

Gritzner, M., Marcus, A., Aspinall, R., Custer, S., 2001. Assessing landslide potential using GIS, soil wetness modeling and topographic attributes, Payette River, Idaho. Geomorphology 37, 149–165.

Hsiao, K.H., Liu, J.K., Yu, M.F., Tseng, Y.H., 2004. Change detection of landslide terrains using ground-based LiDAR data. XXth ISPRS Congress, Istanbul, Turkey, Commission VII, WG VII/5.

Kimura, H., Yamaguchi, Y., 2000. Detection of landslide areas using satellite radar interferometry. Photogrammetric Engineering and Remote Sensing 66 (3), 337–344.

Klinkenberg, B., 1992. Fractals and morphometric measures: is there a relationship? Geomorphology 5, 5–20.

Korup, O., 2004. Landslide-induced river channel avulsions in mountain catchments of southwest New Zealand. Geomorphology 63, 57–80.

Lee, C.A., 1938. Recent landslides in Salmon Creek canyon, Idaho. Journal of Geology 46 (4), 660–665.

Lifton, N., Chase, C., 1992. Tectonic, climatic and lithologic influences on landscape fractal dimension and hypsometry: implications for landscape evolution in the San Gabriel Mountains, California. Geomorphology 5, 77–114.

McKean, J., Roering, J., 2004. Objective landslide detection and surface morphology mapping using high-resolution airborne laser altimetry. Geomorphology 57, 331–351.

Miska, L., Hjort, J., 2005. Evaluation of current statistical approaches for predictive geomorphological mapping. Geomorphology 67, 299–315.

Phillips, J., 2005. Weathering instability and landscape evolution. Geomorphology 67, 255–272.

Rowlands, K., Jones, L., Whitworth, M., 2003. Landslide laser scanning: a new look at an old problem. Quarterly Journal of Engineering Geology and Hydrogeology 36, 155–157.

Smith, L., 2001. Columbia Mountain landslide: late-glacial emplacement and indications of future failure, Northwestern Montana, USA. Geomorphology 41, 309–322.

Turcotte, D., 1997. Fractals and Chaos in Geology and Geophysics, 2nd ed. Cambridge University Press, New York.

Wallace, J., Morris, B., Howarth, P., 2004. The effects of scale on fractal dimension of topography: a case study from Sudbury, Ontario, Canada. Proceedings Geoscience and Remote Sensing Symposium, IEEE International, vol. 5, pp. 2845–2848.

Walsh, S.J., Bian, L., McKnight, S., Brown, D.G., Hammer, E.S., 2003. Solifluction steps and risers, Lee Ridge, Glacier National Park, Montana, USA: a scale and pattern analysis. Geomorphology 55, 381–398.